Formation of local spin-state concentration waves during the relaxation from photoinduced state in a spin-crossover polymer

Céline Mariette, Elzbieta Trzop, Serhane Zerdane, Pierre Fertey, Daopeng Zhang, Francisco J Valverde-Muñoz, José-Antonio J Real, Eric Collet

Formation of local spin-state concentration waves during the relaxation from photoinduced state in a spin-crossover polymer

Authors

Céline Mariette[a], Elzbieta Trzop[a], Serhane Zerdane[a], Pierre Fertey[b], Daopeng Zhang[cd], Francisco J. Valverde-Muñoz[c], José-Antonio Real[c] and Eric Collet[a]*

[a]Institut de Physique de Rennes, UMR 6251, Univ Rennes 1, CNRS, Campus de Beaulieu, Rennes, 35042, France

[b] Synchrotron SOLEIL, BP 48, L'Orme des Merisiers, Saint Aubin, Gif-sur-Yvette Cedex, 91192, France

[c]Instituto de Ciencia Molecular (ICMol), Universidad de Valencia, C/ Catedrático José Beltrán Martínez 2, Paterna, 46980, Spain

[d]College of Chemical Engineering, Shandong University of Technology, Zibo, 255049, People's Republic of China

Correspondence email: eric.collet@univ-rennes1.fr

Synopsis We study how broken symmetry and spin-state concentration waves compete during the relaxation from photoinduced high spin to ground low spin phase of a 2D spin-crossover polymer.

Abstract We report on the complex relaxation from the photoinduced high-spin phase (PIHS) to the low spin phase of the bimetallic 2D coordination spin-crossover polymer $[Fe[(Hg(SCN)_3)_2](4,4'bipy)_2]_n$. During the thermal relaxation, commensurate and incommensurate spin-state concentration wave's (SSCW) form. However, contrary to the steps forming at thermal equilibrium, associated with long-range SSCW order, the SSCWs forming during the relaxation from the PIHS phase correspond to short-range order, revealed by diffuse X-ray scattering. We interpret this as resulting from the competition between the two types of SSCW orders and another structural symmetry breaking, due to ligand ordering, occurring at low temperature and precluding long-range SSCW order.

Keywords: Photo-crystallography; Phase transition; Aperiodicity; Symmetry breaking.

1. Introduction

Advanced crystallography methods have played an important role in material science for connecting their macroscopic properties to microscopic physics or chemistry. It is fair to say that with this regard Philip Coppens has been pioneering different types of developments and applications of the field, such as X-ray charge-density analysis (Koritsanszky & Coppens, 2001). In relation with the present research paper, we can also mention the importance of photo-crystallography and its extension to the time domain (Kim *et al.*, 2002, Chen *et al.*, 2003, Coppens *et al.*, 2010, Coppens, 2015) or the investigation of aperiodic structural modulation, at the origin of unusual electrical conductivity in β-(BEDT-TTF)$_2$I$_3$ (Leung *et al.*, 1985) for example.

Among a wealth of materials, showing various types of functions related to structural reorganizations, and which can be driven by external stimuli, spin-crossover (SCO) molecular crystals (Halcrow, 2013, Real *et al.*, 2005, Bousseksou *et al.*, 2011) are very interesting in terms of structural science related to the emergence of functions. These molecular systems are made up of transition metal atoms in a ligand field, showing bistability between a low (LS) and a high spin (HS) states. A thermal conversion from LS to HS states can occur, as high temperature favors the HS state of higher entropy (Gutlich & Hauser, 1990). Because of the electronic redistribution, the HS state is less bonding and corresponds to a higher molecular volume, due to an important metal-ligand bond elongation (Huby *et al.*, 2004, Pillet *et al.*, 2004, Guionneau, 2014, Kusz *et al.*, 2001, Collet *et al.*, 2006, Collet *et al.*, 2009). This structural deformation, involving macroscopic volume change, plays an important role for the light-induced electronic spin state trapping (LIESST) as well as reverse-LIESST (Decurtins *et al.*, 1985, Goujon *et al.*, 2008, Marchivie *et al.*, 2002, Trzop *et al.*, 2007, Clements *et al.*, 2016, Hauser, 1986). Time-resolved structural studies, including femtosecond XANES and picosecond X-ray diffraction, have shown that SCO crystals excited by a femtosecond laser pulse undergo a complex out-of-equilibrium dynamics. The molecular structural trapping occurs at the molecular level on the 100 fs timescale (Cammarata *et al.*, 2014, Bertoni *et al.*, 2012, Bertoni, Cammarata, *et al.*, 2015, Lemke *et al.*, 2017, Zhang *et al.*, 2014, Tissot *et al.*, 2011). It is followed on the ns timescale by lattice expansion, driven by molecular expansion (Bertoni, Lorenc, Cailleau, *et al.*, 2016, Bertoni, Lorenc, *et al.*, 2015) and on the µs timescale by lattice heating (Collet, Lorenc, *et al.*, 2012, Bertoni, Lorenc, Graber, *et al.*, 2016). P. Coppens helped us going deeper in the time-domain analysis of the structural changes involved, which is difficult to analyze when the molecular conversion rate is low (Collet, Moisan, *et al.*, 2012).

Materials' response to external stimuli is not always as simple as the sum of independent responses of molecules constituting the crystal. In the case of SCO materials, the molecular packing in crystals is associated with elastic coupling between molecules, mediated over long range through the lattice, which can drive cooperative SCO (Buron-Le Cointe *et al.*, 2012, Tissot *et al.*, 2011, Spiering & Willenbacher,

1989, Slimani *et al.*, 2015, Enachescu *et al.*, 2015, Nicolazzi *et al.*, 2008). On short range, the molecular packing and the elastic energy costs, related to important structural changes, can also be at the origin of elastic frustration (Watanabe *et al.*, 2016, Paez-Espejo *et al.*, 2016). It can generate stepwise conversions of the fraction of HS molecules γ_{HS} with temperature, as recently discussed in recent reviews (Shatruk *et al.*, 2015, Ortega-Villar *et al.*, 2016). Structural studies of several Fe^{II} systems have reported periodic and aperiodic long-range order of LS and HS states (Boinnard *et al.*, 1994, Chernyshov *et al.*, 2003, Huby *et al.*, 2004, Reger *et al.*, 2001, Money *et al.*, 2007, Luan *et al.*, 2015, Yamada *et al.*, 2006, Sato *et al.*, 2009, Brefuel *et al.*, 2010, Brefuel *et al.*, 2009, Collet, Watanabe, *et al.*, 2012, Bonnet *et al.*, 2008, Clements *et al.*, 2016, Pillet *et al.*, 2012). In addition, similar HS-LS ordering phenomena were reported for a reduced number of Fe^{III} (Griffin *et al.*, 2011, Li *et al.*, 2013, Vieira *et al.*, 2013, Murnaghan *et al.*, 2014, Harding *et al.*, 2015) Co^{II} (Bhar *et al.*, 2012) and Mn^{III} (Fitzpatrick *et al.*, 2015) complexes. This long-range ordering of molecules in HS and LS states corresponds to the formation of spin-state concentration waves, i.e. a periodic spatial modulation of the probability for a crystalline site to populate the HS state (Collet, Watanabe, *et al.*, 2012, Marino *et al.*, 2015, Watanabe *et al.*, 2016, Trzop *et al.*, 2016).

We have recently reported a multi-step thermal equilibrium conversion process from complete HS to complete LS phases, in the bimetallic 2D coordination polymer $[Fe[(Hg(SCN)_3)_2](4,4'bipy)_2]_n$ associated with different intermediate phases with different HS-LS long-range orders on the steps. This multi-step conversion shows therefore similar features to Devil's staircase-type phase transition in the γ_{HS}-*vs*-T conversion (Trzop *et al.*, 2016). In addition, more conventional structural phase transition, related to symmetry breaking related to molecular distortion and/or ligand ordering, can also occur in SCO materials and be coupled or not to the change of spin state (Watanabe *et al.*, 2013, Brefuel *et al.*, 2010, Brefuel *et al.*, 2009). Here we present a detailed structural analysis of the SCO phenomena in the bimetallic 2D coordination polymer $[Fe[(Hg(SCN)_3)_2](4,4'bipy)_2]_n$ (**1**). We briefly summarize thermal equilibrium phase transitions and the structural nature of their changes, to focus on the multi-step relaxation process from the photoinduced HS state.

2. Phase transitions at thermal equilibrium for (1)

The multistep spin state conversion of the two-dimensional (2D) bimetallic coordination polymer (**1**) is illustrated by the thermal dependence of $\chi_M T$ product (χ_M = magnetic susceptibility, T temperature) shown in Fig. 1. It is governed by the thermal population of the diamagnetic LS and paramagnetic HS states and is consequently scaled to the evolution of the fraction of molecules in the HS state γ_{HS}. Magnetic measurements and crystallographic studies revealed different phases and their crystalline structures, already presented in detail elsewhere (Trzop *et al.*, 2016, Zhang, Trzop, Valverde-Muñoz, *et al.*, 2017), are schematically represented in Fig. 1.

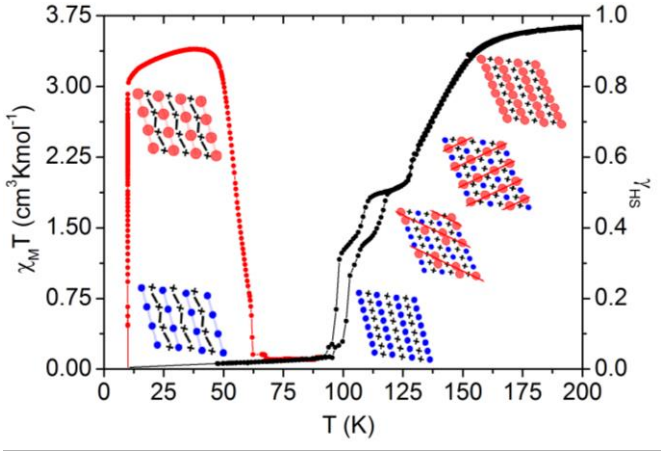

Figure 1 Temperature dependence of $\chi_M T$ (left axis), scaled to HS fraction γ_{HS} (right axis) in the 10–300 K range at thermal equilibrium for (**1**) (black curves) and in the warming mode after photoexcitation at 10 K by a laser at 660 nm (red curve). The different structures of the bimetallic coordination polymer made of Fe^{II} (HS=red, LS=bleu spheres) and Hg^{II} (crosses) connected by (4,4'bipy) ligands (lines) are schematically represented, with stripes (red lines) forming on the steps. The $\chi_M T$ scaling to γ_{HS} is not valid in the LIESST regime at very low temperature owing to zero field splitting of the paramagnetic HS species.

In the interval 300-190 K, $\chi_M T \approx 3.67$ cm^3 K mol^{-1} corresponds to a phase where the Fe^{II} centers are in the HS (S = 2, γ_{HS} = 1) state. This is the high spin (HS) high symmetry (hs) phase (HS^{hs} $P\bar{1}$). In the crystalline structure, there is a single Fe^{II} site lying on an inversion center. In the HS^{hs} phase, the asymmetric unit consists of one axially coordinated N atom belonging to a 4,4'-bipy ligand and two equatorial N atoms belonging to two crystallographically distinct NCS groups (Figure 2). The average Fe1-N bond length of the [$Fe^{II}N_6$] octahedron, <Fe1-N> = 2.158(3) Å, is typical for Fe^{II} atoms in the HS state. Below 170 K, $\chi_M T$ drops rapidly towards a plateau in the [108-125 K] range, indicating that 50% of the Fe sites are in the HS and in the LS states. We have shown that a symmetry breaking occurs on the plateau (Trzop *et al.*, 2016). This cell doubling is characterized by the appearance of superstructure Bragg peaks at $\boldsymbol{q_c}=\frac{1}{2}\boldsymbol{a}^*+\frac{1}{2}\boldsymbol{b}^*+\frac{1}{2}\boldsymbol{c}^*$, where $\boldsymbol{a}^*$,$\boldsymbol{b}^*$ and $\boldsymbol{c}^*$ refer to the reciprocal lattice of the high symmetry phase. The structural refinement reveals two different Fe sites: site 1 is mainly LS as characterized by <Fe1-N>≈1.962(3) Å, whereas site 2 is mainly HS with <Fe2-N>≈2.146(3) Å. The structure consists then of stripes of molecules in mainly HS or LS states and alternating along $\boldsymbol{q_c}$ in a ...HS-LS-HS-LS... sequence (Figure 3,a). This spin-state concentration wave, commensurate with the high symmetry lattice, corresponds to a spatial modulation of the HS fraction:

SSCW^{com}: $\gamma_{HS}^{c}(r) = \gamma_{HS}^{c}+(\eta^{c}/2)\times\cos(\boldsymbol{q_c}.\boldsymbol{r})$

where X-ray studies give $\gamma_{HS}^{c} \approx 0.5$ and $\eta^{c}\approx 0.9$ (Trzop *et al.*, 2016) at 117 K.

On cooling further, a second plateau appears in the interval 96-108 K, where an incommensurate modulation appears, characterized by satellite reflections at $\boldsymbol{q_i}$ = 0.48$\boldsymbol{a^*}$+0.35$\boldsymbol{b^*}$+0.42$\boldsymbol{c^*}$. Superspace crystallography evidenced that it corresponds to a phase where the spatial modulation of the HS fraction is incommensurate with the lattice (Figure 3, b). This spin-state concentration wave, incommensurate with the molecular packing, is described as follows:

SSCW^{incom}: $\gamma_{HS}^{i}(\boldsymbol{r}) = \gamma_{HS}^{i}+(\eta^{i}/2)\times\cos(\boldsymbol{q_i}.\boldsymbol{r})$

with γ_{HS}^{i}=0.34 and η^{i}=0.85 at 102 K. Since there is no group-subgroup relationship between the SSCW^{com} and the SSCW^{incom}, the transition between the two phases is reconstructive and first-order. These features related to the formation of different long-range ordered HS-LS sequences on the thermal steps present some analogies with Devil's staircase-type transformations (Bak & von Boehm, 1980, Fisher & Selke, 1980, Aubry, 1983, Bak & Bruinsma, 1982, Ohwada *et al.*, 2001, Collet *et al.*, 2001). q_s continuously changes from (0.47 0.32 0.41) at 96 K, to (0.40 0.41 0.44) at 108 K, above which the locking at (½ ½ ½) occurs (Trzop *et al.*, 2016).

Below ≈ 95 K the system reaches the low spin phase of high symmetry (LS^{hs}), which is isostructural to the HS^{hs} phase. The unique Fe site is now LS with <Fe1-N> = 1.961(3) Å at 90 K. Apart from these intra-molecular metric changes, driving volume change, the LS^{hs} structure does not present other relevant differences with respect to the HS^{hs} structure at 220 K (Figure 2).

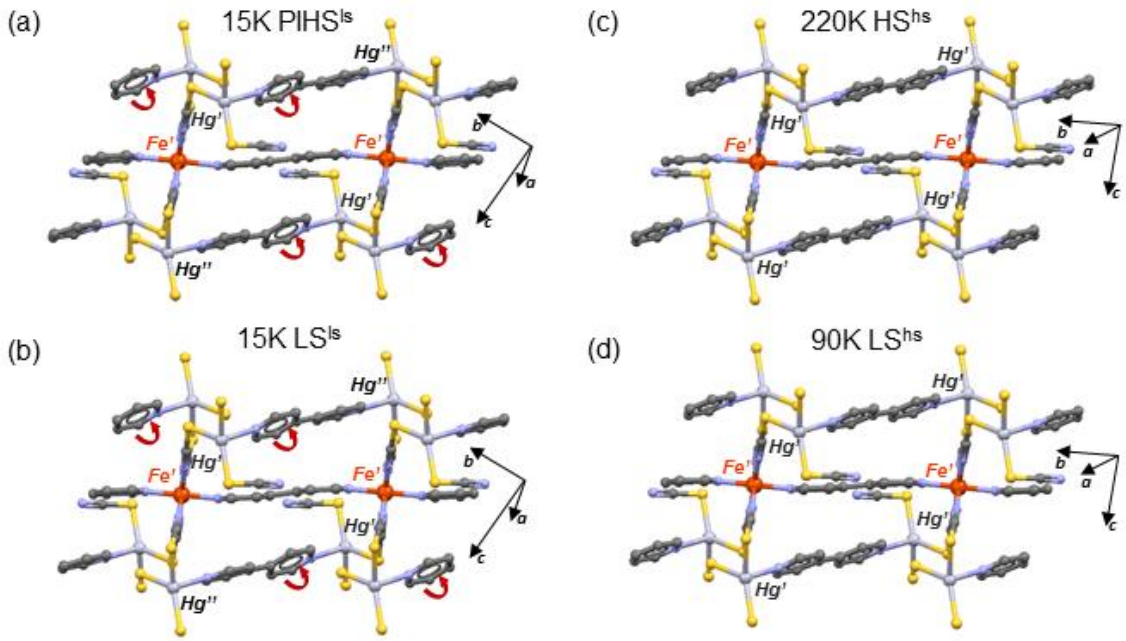

Figure 2 Structures of the isostructural high symmetry HS^{hs} (220 K) and LS^{hs} (90 K) phases and of the isostructural PIHS^{ls} (15 K) and LS^{ls} (15 K) phases. The symmetry breaking is associated with ligand ordering (titling of bpy). The unit cell axis are given in the high and low symmetry cells. PIHS^{ls} and LS^{ls} stand for photo-induced HS low symmetry (ls) and LS low symmetry (ls) phases.

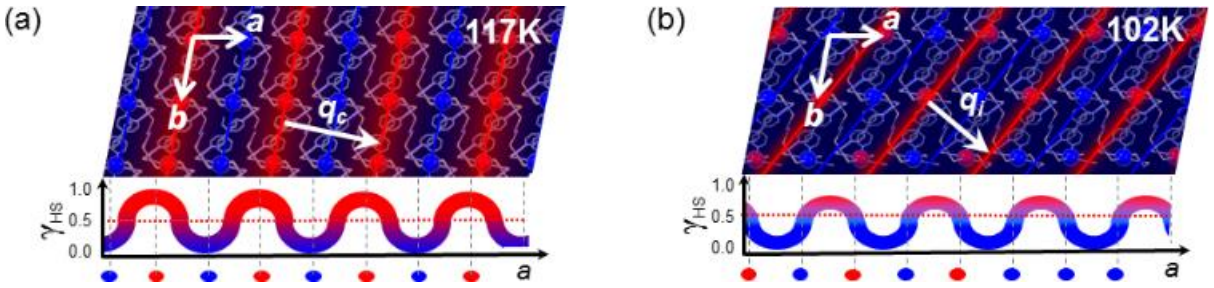

Figure 3 The commensurate spin-state concentration wave SSCW^{com} forming along $\boldsymbol{q_c}$ (117 K, left) and incommensurate SSCW^{incom} (102 K, right) forming along $\boldsymbol{q_i}$ (projected), showing HS (red) and LS (blue) stripes. The scheme below show spatial evolution of γ_{HS} over crystalline sites.

3. Ligand ordering in low symmetry low spin and photoinduced high spin phases

Below 85 K, a structural symmetry breaking occurs towards a low symmetry LS phase (LS^{ls}) (Zhang, Trzop, Valverde-Munoz, *et al.*, 2017). It corresponds to another unit-cell doubling with respect to the high symmetry HS^{hs} and LS^{hs} unit cells, with the appearance of Bragg peaks at $\boldsymbol{q_L}$ =1/2**b***+1/2**c***. In this doubled unit cell, the [Fe(μ-4,4'-bipy)]$_n^{2+}$ chains are made of non centrosymmetric Fe^{II} sites linked by planar centrosymmetric 4,4'-bipy bridges, while the [[Hg(SCN)$_3$]$_2$(μ-4,4'-bipy)]$_2$ units are constituted of two crystallographically distinct Hg(1,2) centers bridged by a non centrosymmetric 4,4'-bipy bridge. Consequently, several structural rearrangements occur as shown in Figure 2. The main feature related to this symmetry breaking is the relative twisting of the pyridine rings bridging the two Hg sites while pyridine rings of Fe sites remain planar in the LS^{ls} phase. This is due to the fact that with the cell doubling the inversion symmetry between the pyridine rings connecting the Fe atoms remain, whereas the one between the pyridine rings connecting the Hg atoms are lost.

We have also reported that the system undergoes LIESST: the magnetic susceptibility of a LS sample at 10 K increases from $\chi_M T \approx 0.09$ cm^3 K mol^{-1} and saturates around 3.0 cm^3 K mol^{-1} after irradiation with red light (λ = 633 nm) (Zhang, Trzop, Valverde-Munoz, *et al.*, 2017). Once the light irradiation is stopped and the temperature is increased, at a rate of 0.3 K min^{-1}, $\chi_M T$ reaches a maximum around 3.40 cm^3 K mol^{-1} at 38 K. It is characteristic of the thermal population of the different microstates arising from the zero-field splitting of the photoinduced HS phase (PIHS, S = 2). Interestingly, the structure of the photoinduced HS state is not the same as the one of the fully HS state existing at thermal equilibrium above 220 K. Previous photocrystallographic studies have shown that with respect to the HS^{hs} structure, the photoinduced state has a low symmetry. The structure of this PIHS^{ls} state is isostructural to the LS^{ls} phase, also characterized by the presence of Bragg peaks at $\boldsymbol{q_L}$ =1/2***b****+1/2***c**** with respect to the HS^{hs}. The unit cell also contains a single non-centrosymmetric Fe^{II} site with an average Fe-N bond length

<Fe1-N> = 2.141(3) Å, characteristic of the formation of the HS state. This symmetry breaking is also associated with the twisting of the pyridine rings connecting the Hg atoms, as for the LS^{ls} phase (Figure 2). More details about the LS^{ls} and $PIHS^{ls}$ crystalline structures can be found in (Zhang, Trzop, Valverde-Munoz, *et al.*, 2017).

During the thermal relaxation above 39 K, the magnetic susceptibility drops rapidly and reaches back the initial value characteristic of the LS state around 62 K, indicating a complete relaxation from PIHS to LS states. However, this thermal relaxation does not occur in a single step. The derivative curve (Figure 4) indicates that the relaxation rate is not monotonous, as it is slowing down in the 50-60 K range, where $\gamma_{HS}\approx0.5$ and $\gamma_{HS}\approx0.33$ are characteristic of steps observed during the thermal crossover, and gets faster around 60 K. It therefore appears of interest to go deeper in the analysis of the relaxation process from the $PIHS^{ls}$ phase to track the formation of SSCW during the relaxation process and to compare the structural orders with the ones observed at thermal equilibrium.

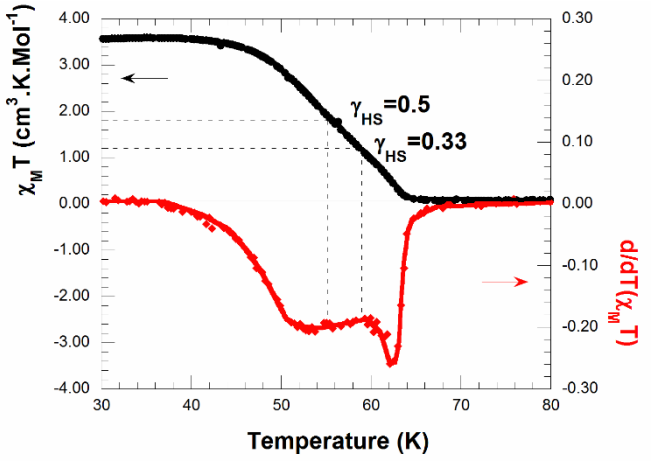

Figure 4 Temperature dependence of $\chi_M T$ in the 30–80 K range in the warming mode after photoexcitation at 10 K by a laser at 633 nm (black). The derivative with temperature (red) shows a slower relaxation in the 50-60 K range and a faster relaxation above 60 K towards the LS state.

4. Multi-step thermal conversion *vs* thermal relaxation from photoinduced high spin state

In order to study in detail the structural changes involved in the processes, we performed X-ray diffraction experiments at synchrotron SOLEIL at the CRISTAL beamline. Single crystal measurements were performed at different temperature, before and after light irradiation. We investigated both the thermal phase transitions and the relaxation process from the $PIHS^{ls}$ phase through the evolution of the Bragg peaks and diffuse scattering. We used a He-flow cryojet (Cryocool G2b LT from Cryo Industries of America) to cool the sample down to 20 K, where the $PIHS^{ls}$ phase has a lifetime much larger than 1h. It is then easy to generate the $PIHS^{hs}$ state with laser excitation, at 633 or

658 nm (Zhang, Trzop, Valverde-Munoz, *et al.*, 2017) or at 532 nm in the present work, and to collect then X-ray diffraction data on the diffractometer (Newport-Rigaku Oxford Diffraction, equipped with the Atlas detector). For data analysis, we used the Crysalis software. The wavelength was tuned at 0.513450 Å, using a Si 111 double crystal monochromator and sagitale focalization. The unit cell parameters and orientation matrix were refined using *CrysAlisPro* software (Rigaku, 2015). In order to extract the intensity profile along very precise directions, we adopted a two-step method. After unit cell refinements, parallel (***a****, ***b****) reciprocal planes were reconstructed with a resolution of 0.002 $Å^{-1}$ along the b* direction. Then, intensity was averaged over 20 unit cells to reconstruct a 3D reciprocal unit. Profiles were extracted after a subsequent refinement of the basis vector in the averaged unit cell. In order to increase the contrast, diffuse scattering profiles were analyzed after filtering from major parasite reflections and Bragg peaks.

The $SSCW^{com}$ forming on the plateau at $\gamma_{HS} \approx 0.5$ at thermal equilibrium is characterized by the appearance of superstructure Bragg peaks at $\boldsymbol{q}_c=\frac{1}{2}\boldsymbol{a}^*+\frac{1}{2}\boldsymbol{b}^*+\frac{1}{2}\boldsymbol{c}^*$. Figure 5 shows that these superstructure peaks are as sharp as general Bragg peaks and characteristic of a long-range ordered $SSCW^{com}$. In a similar way, the satellite reflections at $\boldsymbol{q}_i = 0.48\boldsymbol{a}^*+0.35\boldsymbol{b}^*+0.42\boldsymbol{c}^*$ (102 K, Figure 5), which appear on the low temperature plateau, are also sharp and related to the aperiodic but long-range $SSCW^{incom}$. The fit used Gaussian functions with similar FWHM (0.008 ± 0.002 $Å^{-1}$) for the different peaks. This width is mainly limited by the experimental resolution. It is important to recall that the symmetry at T = 95K is the same as the high symmetry one, which is reflected in the diffraction image by the fact that the scattered intensity at $\boldsymbol{q}_c$ and $\boldsymbol{q}_i$ completely vanish. Below 85 K, new superstructure Bragg peaks appear at $\boldsymbol{q}_L = 1/2\boldsymbol{b}^*+1/2\boldsymbol{c}^*$, which are characteristic of the symmetry breaking in the LS^{ls} phase, associated with twisting of the pyridine rings. These peaks measured here at 30 K (Figure 6) are also as sharp as general Bragg peaks, leading us to conclude again to a long-range ligand order at low temperature. The fit in Figure 6 used Gaussian functions for Bragg peaks and superstructure reflections, with similar FWHM (0.007 ± 0.002 $Å^{-1}$). The later value defines our experimental resolution which is comparable with the one measured on our laboratory set-up.

The photoswitching, evidenced by magnetic measurements, from LS^{ls} to $PIHS^{ls}$ is characterized by a structural distortion without symmetry breaking. X-ray diffraction measurements allowed to extract a volume increase around 25 $Å^3$ (Figure 7), related to the increase of the Fe-N bonds between LS and HS states. This volume change is comparable with the ≈35 $Å^3$ volume increase from LS (90 K) to HS (300 K), which also includes thermal contraction in addition to lattice contraction due to bond shrinking during the spin state conversion. It is responsible for the shift of the Bragg peaks after photo-excitation, as seen in Figure 6. The volume contraction observed on warming is characteristic of the relaxation towards the low spin state and the superstructure peaks at $\boldsymbol{q}_L$ indicate the relaxation towards the LS^{ls} phase. The volume change in the LS state between 30 and 70 K corresponds to the expected thermal

exapnsion. However, the lattice volume in the 55-65 K range is significantly lower than the volume of the LS state at 30 or 70 K. The 55-65 K range corresponds to the intermediate state forming during the relaxation. It is very likely that the elastic frustration, at the origin of the formation of (local) SSCW, results in a more compact structure.

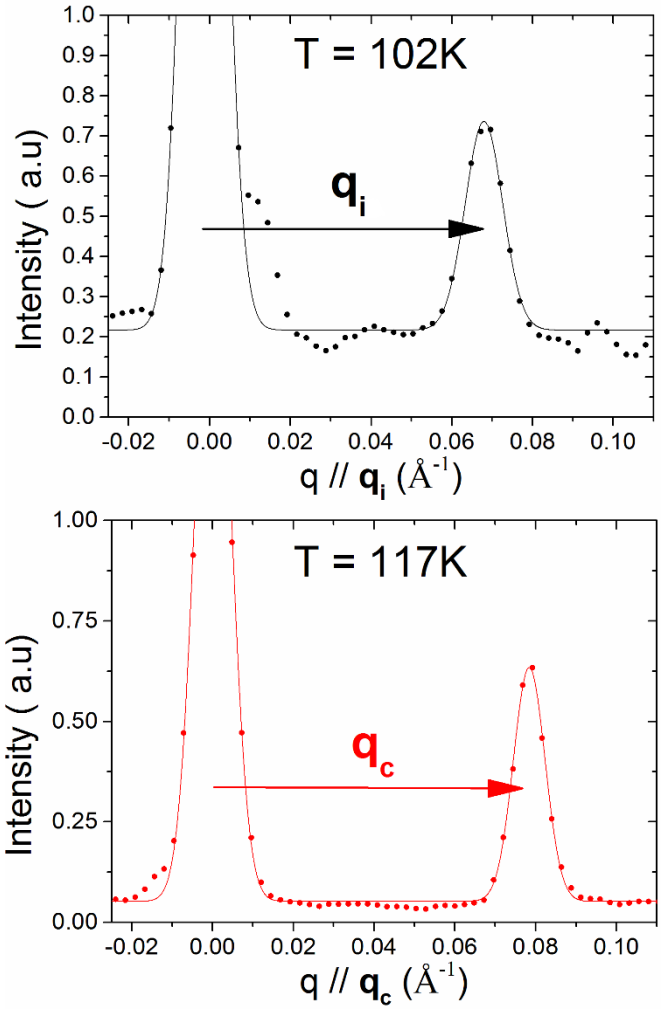

Figure 5 Reconstructed diffracted X-ray intensity in reciprocal spaces, showing sharp superstructure Bragg peaks at $\boldsymbol{q_c} = \frac{1}{2}\boldsymbol{a}^* + \frac{1}{2}\boldsymbol{b}^* + \frac{1}{2}\boldsymbol{c}^*$ at 117 K, related to the formation of the SSCW^{com} on the plateau where $\gamma_{HS} \approx 0.5$. The sharp satellite reflections observed at $\boldsymbol{q_i} = 0.48\boldsymbol{a}^* + 0.35\boldsymbol{b}^* + 0.42\boldsymbol{c}^*$ at 102 K are related to the formation of the SSCW^{incom} on the plateau where $\gamma_{HS} \approx 0.34$.

It starts at around 45 K and goes on in a non-monotonous way up ≈ 60 K, where the initial volume of the LS state is reached anew. The volume change during the relaxation from the photoinduced HS state occurs at temperatures in good agreement with magnetic data (Figure 4), and a kind of plateau or slowing down during the relaxation around 50-55 K. These temperatures correlate well with the magnetic data where the relaxation slows down in this temperature range.

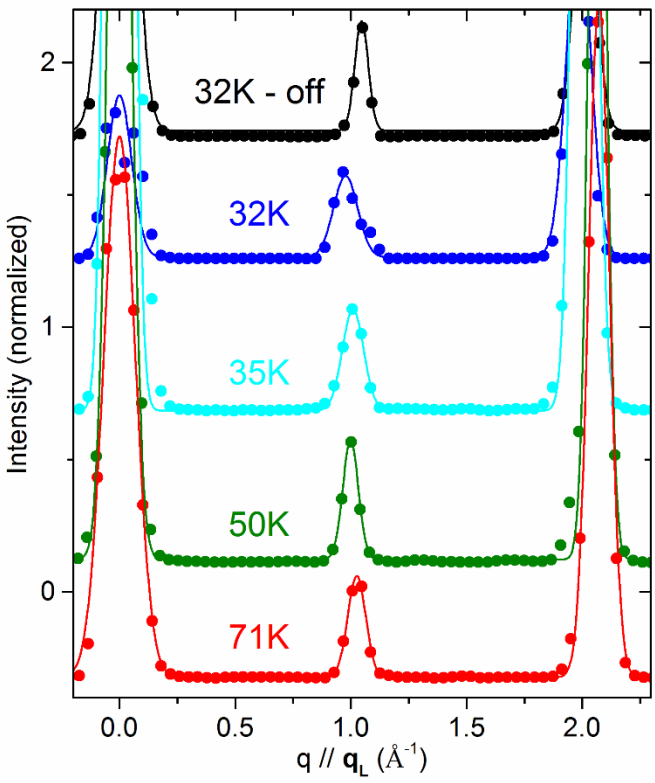

Figure 6 Diffracted X-ray intensity along $\boldsymbol{q}_L$ between Bragg peaks, showing similar sharp superstructure peaks at $\boldsymbol{q}_L = \frac{1}{2}\boldsymbol{b}^* + \frac{1}{2}\boldsymbol{c}^*$ at 32 K in the LS^{ls} and PIHS^{ls} and at higher temperature during the thermal relaxation from PIHS^{ls} state. The shift of the Bragg peaks along $\boldsymbol{q}_L$ from the reference Bragg peak at q=0 is due to lattice expansion at 32 K before and after laser excitation and contraction during relaxation from PIHS.

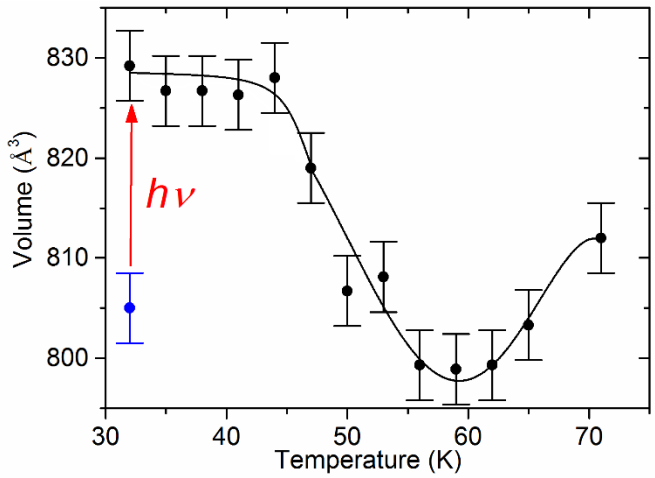

Figure 7 Evolution of the unit-cell volume at 32 K from LS^{ls} to PIHS^{ls} with laser irradiation at 532 nm, and during the thermal relaxation towards the LS^{ls} at higher temperature.

The analysis of the diffraction signal in the reciprocal space provides key information on the structural processes involved during the relaxation from the $PIHS^{ls}$ phase towards the LS^{ls} phase. On one hand, it should be underlined that the superstructure Bragg peaks, observed at $\boldsymbol{q_L}$ =1/2$\boldsymbol{b^*}$+1/2$\boldsymbol{c^*}$, are always present during the relaxation (Figure 6). We could not detect significant change in the width of these superstructure peaks related to the ligand ordering. We therefore conclude that the photo-switching process, which involves mainly Fe-N elongation, does not induce ligand disorder. Ligands are probably frozen at such low temperature. On the other hand, we observe important scattering signal around $\boldsymbol{q_c}$ and $\boldsymbol{q_i}$ during the relaxation process (Figures 8 & 9). X-ray scattering at these specific positions in the reciprocal space is characteristic of the formation of $SSCW^{com}$ and $SSCW^{incom}$. However, we do not observe sharp satellite or superstructure Bragg peaks, contrary to what is observed at thermal equilibrium (Figure 5). Instead, diffuse scattering is observed around $\boldsymbol{q_c}$ and $\boldsymbol{q_i}$ in the 47-56 K range. At 59 K this diffuse scattering signal around $\boldsymbol{q_c}$ and $\boldsymbol{q_i}$ disappears.

The diffuse scattering around $\boldsymbol{q_c}$ and $\boldsymbol{q_i}$ are reminiscence of the spatial fluctuation of the symmetry breaking order parameters and reveal the local formation of the $SSCW^{com}$ and $SSCW^{incom}$. The coexistence of diffuse signal at both $\boldsymbol{q}$ vector at all temperature results is a complicated peanuts like shape of the diffuse scattering (Figure 8). 3D fitting of this shape with 3 ellipsoids was not possible due to overparametrization. Nevertheless, the resulting iso-intensity surfaces are well reproduced by considering an isotropic pattern around $\boldsymbol{q_i}$ and a disk shaped from around $\boldsymbol{q_c}$. Profiles were extracted around $\boldsymbol{q_i}$ and $\boldsymbol{q_c}$ directions (figure 9). Due to the interpenetration of the ellipsoids, 2 maxima are systematically observed at $\boldsymbol{q_i}$ and 3 maxima at $\boldsymbol{q_c}$. We used Lorentzian functions to fit the diffuse signal along *q:*

$$I(q) = I_0 + \frac{I_M}{1 + (q - q_c)^2 {\xi_i}^2}$$

where q is the absolute scattering vector along the considered direction, q_c is the critical vector, and ξ_i the correlation lengths along different directions i. The broader diffuse scattering at 45 K corresponds to correlation extending over ≈ 2 unit cells, whereas the sharper diffuse scattering around 51 K corresponds to correlation extending over ≈11 unit cells.

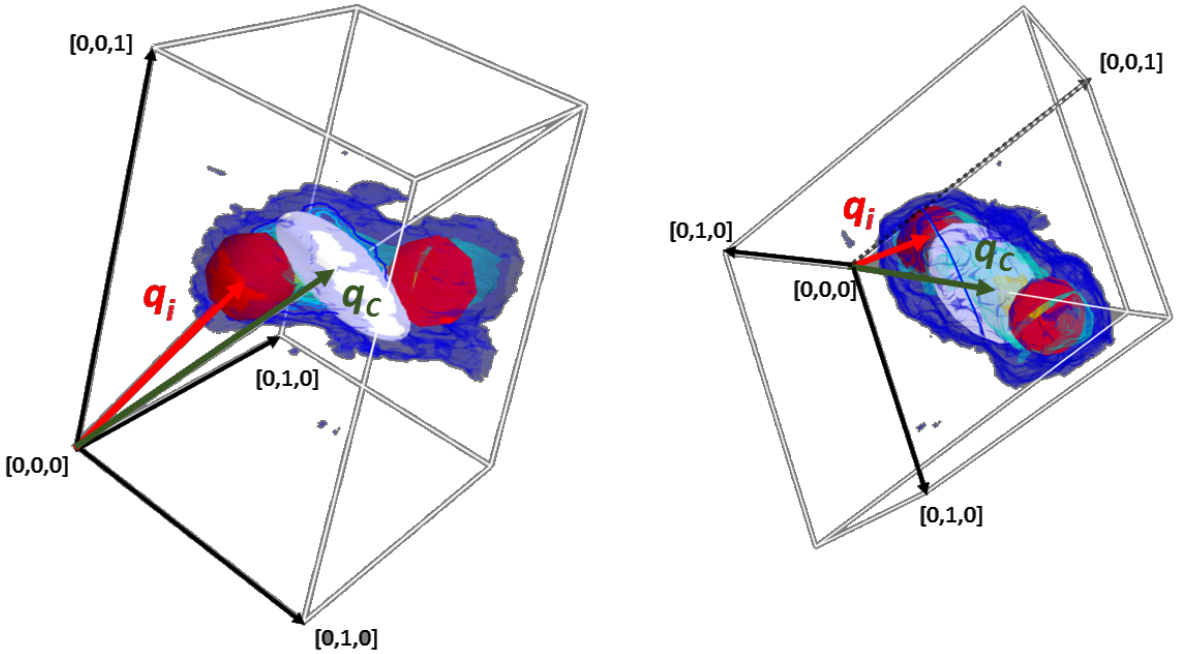

Figure 8 3D reconstruction of the diffuse scattering at T = 53K. Red sphere and white ellipsoid are constructed to fit the diffuse scattering shape observed around respectively $\boldsymbol{q_i}$ and $\boldsymbol{q_c}$. The white box represents the edges of the reciprocal unit cell and is given by the position of the general Bragg peaks, which are not shown for clarity. This figure enhances the anisotropic shape of the diffuse X-ray scattering around $\boldsymbol{q_c} = \frac{1}{2}\boldsymbol{a}^* + \frac{1}{2}\boldsymbol{b}^* + \frac{1}{2}\boldsymbol{c}^*$ and isotropic shape around $\boldsymbol{q_i} = 0.48\boldsymbol{a}^* + 0.35\boldsymbol{b}^* + 0.42\boldsymbol{c}^*$.

This result can be discussed in regard to a previous study of the stepwise relaxation of another SCO material, where clear X-ray diffraction Bragg peaks signing the long-range formation of HS-LS sequence was revealed on the relaxation step (Pillet *et al.*, 2012). Our case constitutes a next step in complexity. The first reason is the multistep ordering happening during the thermal conversion. But the key point is certainly the symmetry breaking, associated with the twist of the ligand, arising at low temperature. This was not the case in the study reported by Pillet et al., where HS and PIHS states had exactly the same symmetry. The symmetry breaking we observe below 85K is associated with the ligand ordering along $\boldsymbol{q_L}$ and characterized by a first symmetry breaking order parameter. It should be underlined that this symmetry breaking order parameter has different symmetry from the one related to the formation of the $SSCW^{com}$ ($\boldsymbol{q_c}$) or of the $SSCW^{incom}$ ($\boldsymbol{q_i}$). Therefore, reaching the $SSCW^{com}$ or $SSCW^{incom}$ phase from the $PIHS^{ls}$ phase implies a reconstructive phase transition, as there is no group-subgroup relationship between these phases.

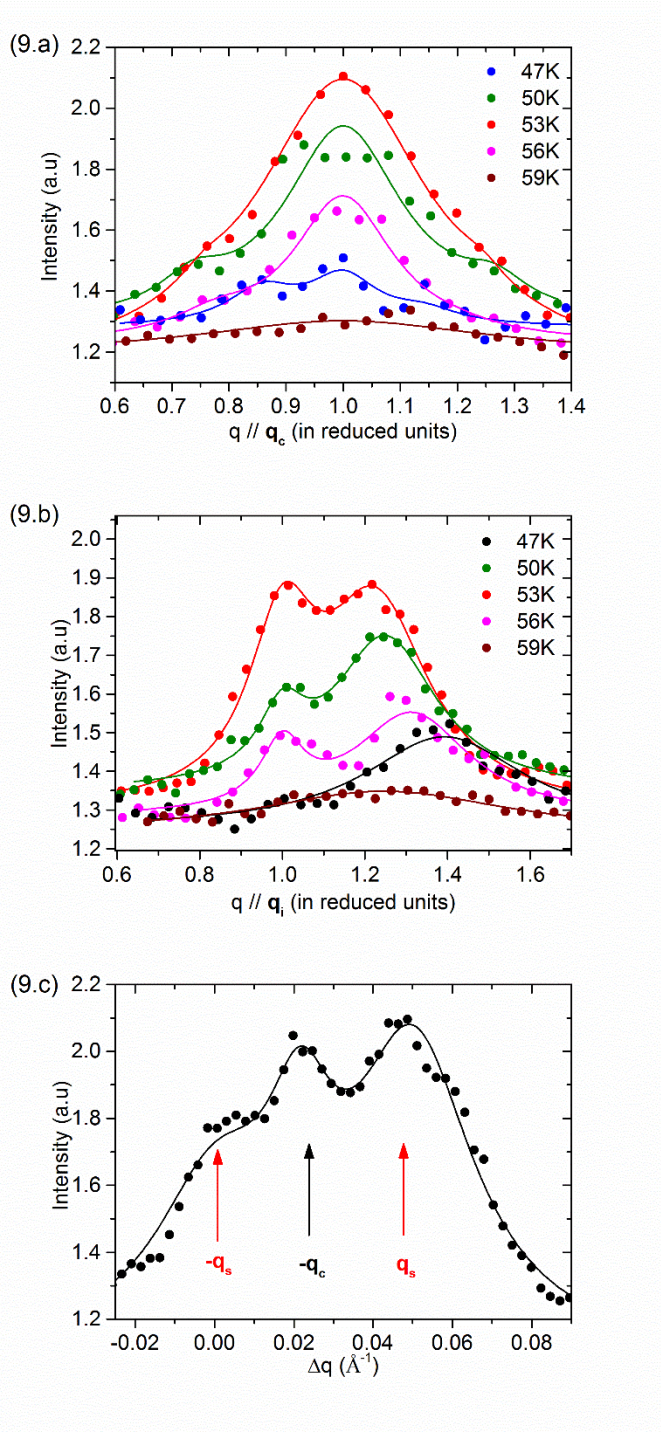

Figure 9 Intensity profiles of the diffuse scattering around $\boldsymbol{q_c} = \frac{1}{2}\boldsymbol{a}^* + \frac{1}{2}\boldsymbol{b}^* + \frac{1}{2}\boldsymbol{c}^*$ (9.a) and $\boldsymbol{q_i} = 0.48\boldsymbol{a}^* + 0.35\boldsymbol{b}^* + 0.42\boldsymbol{c}^*$ (9.b) extracted from intensity volume as shown on figure 8. Continuous lines are the result of a fit with two or three lorentzian functions respectively. Fig. c show a profile along the direction ($+\boldsymbol{q_i}$, $-\boldsymbol{q_i}$) at T = 53K confirming the presence of 3 maxima.

Such first-order transition requires important thermal energy. On the other hand, a recent theoretical study underlined that the step may hardly appear during the relaxation process because the long-range HS-LS order is difficult to form (Watanabe *et al.*, 2016). This energy barrier, in addition to the two competing ordering phenomena between the formation of local SSCW^{com} (around $\boldsymbol{q_c}$) and local SSCW^{incom} (around $\boldsymbol{q_i}$) explains the local character of the SSCW observed during the relaxation. The fit of the diffuse scattering appears in this case to be very challenging due to strong overlap of the signatures at q_c and q_s. Considering the crystallographic directions, we could estimate the extent of the order between 2 and 11 unit cells depending on the direction and the temperature. One should keep in mind that the proper axis of the diffuse scattering ellipsoid, which cannot be determined precisely for the aforementioned reason, do not lye along the crystallographic directions. The formation of small domains might be explained by mismatch domain walls between SSCW^{com} and SSCW^{incom} and/ or antiphase boundaries associated with a spatial phase-shift of the SSCW, as represented schematically on figure 10. These "stacking faults", preclude long-range order.

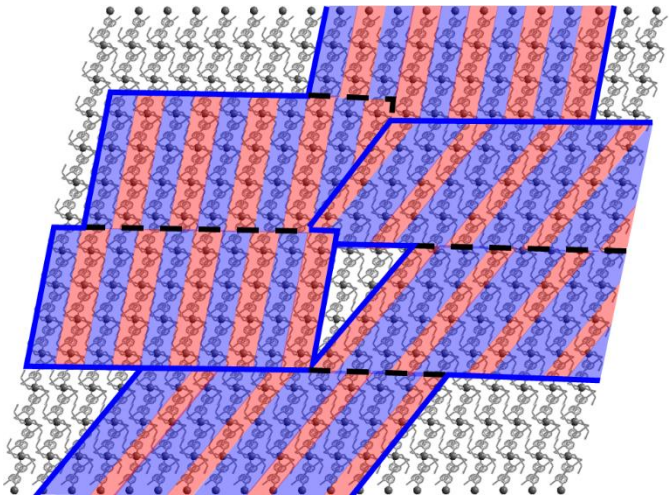

Figure 10 Schematic representation of the formation of locally ordered SSCW^{com} where HS (red) and LS (blue) states alternate on the crystalline sites and SSCW^{incom} domains. Local order may result from the formation of antiphase boundaries (discontinuous lines) between the same "phases" and domain walls (continuous lines) between SCCW^{com} and SSCW^{incom} domains.

5. Conclusion

Phase transitions related to spin-crossover phenomena, at thermal equilibrium or during the relaxation from photoinduced HS state to LS state, are in most cases single-step and isostructural processes. Sometimes more complicated phase transitions may occur, involving symmetry breaking and/or formation of SSCW. Diffraction techniques are powerful to reveal the nature of the symmetry breaking and the structural changes involved (intra and/or intermolecular). The present study reveals an unusual relaxation process from photoinduced HS state, where HS-LS sequences spatially form, but on short-range order only, as directly evidenced by the appearance of diffuse scattering signal. This type of measurement opens new possibilities to investigate, beyond the average crystalline structure, out-of-equilibrium transformations of materials (Guerin *et al.*, 2010), especially when induced by light excitation.

Acknowledgements This work was supported by the Spanish Ministerio de Economia y Competitividad (MINECO), FEDER (CTQ2013-46275-P and CTQ2016-78341-P), Unidad de Excelencia MDM-2015-0538, the Generalitat Valenciana through PROMETEO/2016/147. F.J.V.M. thanks MINECO for a predoctoral (FPI) grant. D.Z. thanks the support from the Natural Science Foundation of China (21671121). E.T. thanks CNRS for Post-Doc funding. EC thanks the National Research Agency (ANR-13-BS04-0002) and Rennes Metropole for equipment funding.

References

Aubry, S. (1983). *J. Phys. France* **44**, 147-162.
Bak, P. & Bruinsma, R. (1982). *Physical Review Letters* **49**, 249-251.
Bak, P. & von Boehm, J. (1980). *Physical Review B* **21**, 5297-5308.
Bertoni, R., Cammarata, M., Lorenc, M., Matar, S. F., Letard, J. F., Lemke, H. T. & Collet, E. (2015). *Acc Chem Res* **48**, 774-781.
Bertoni, R., Lorenc, M., Cailleau, H., Tissot, A., Laisney, J., Boillot, M. L., Stoleriu, L., Stancu, A., Enachescu, C. & Collet, E. (2016). *Nat Mater* **15**, 606-610.
Bertoni, R., Lorenc, M., Graber, T., Henning, R., Moffat, K., Létard, J. F. & Collet, E. (2016). *Crystengcomm* **18**, 7269-7275.
Bertoni, R., Lorenc, M., Tissot, A., Boillot, M. L. & Collet, E. (2015). *Coordination Chemistry Reviews* **282-283**, 66-76.
Bertoni, R., Lorenc, M., Tissot, A., Servol, M., Boillot, M. L. & Collet, E. (2012). *Angew Chem Int Ed Engl* **51**, 7485-7489.
Bhar, K., Khan, S., Costa, J. S., Ribas, J., Roubeau, O., Mitra, P. & Ghosh, B. K. (2012). *Angewandte Chemie International Edition* **51**, 2142-2145.
Boinnard, D., Bousseksou, A., Dworkin, A., Savariault, J. M., Varret, F. & Tuchagues, J. P. (1994). *Inorganic Chemistry* **33**, 271-281.
Bonnet, S., Siegler, M. A., Costa, J. S., Molnar, G., Bousseksou, A., Spek, A. L., Gamez, P. & Reedijk, J. (2008). *Chem Commun*, 5619-5621.
Bousseksou, A., Molnar, G., Salmon, L. & Nicolazzi, W. (2011). *Chemical Society Reviews* **40**, 3313-3335.
Brefuel, N., Collet, E., Watanabe, H., Kojima, M., Matsumoto, N., Toupet, L., Tanaka, K. & Tuchagues, J. P. (2010). *Chemistry* **16**, 14060-14068.
Brefuel, N., Watanabe, H., Toupet, L., Come, J., Matsumoto, N., Collet, E., Tanaka, K. & Tuchagues, J. P. (2009). *Angew Chem Int Ed Engl* **48**, 9304-9307.
Buron-Le Cointe, M., Hébert, J., Baldé, C., Moisan, N., Toupet, L., Guionneau, P., Létard, J. F., Freysz, E., Cailleau, H. & Collet, E. (2012). *Physical Review B* **85**.
Cammarata, M., Bertoni, R., Lorenc, M., Cailleau, H., Di Matteo, S., Mauriac, C., Matar, S. F., Lemke, H., Chollet, M., Ravy, S., Laulhe, C., Letard, J. F. & Collet, E. (2014). *Physical Review Letters* **113**, 227402.
Chen, L. X., Shaw, G. B., Novozhilova, I., Liu, T., Jennings, G., Attenkofer, K., Meyer, G. J. & Coppens, P. (2003). *Journal of the American Chemical Society* **125**, 7022-7034.
Chernyshov, D., Hostettler, M., Tornroos, K. W. & Burgi, H. B. (2003). *Angew Chem Int Ed Engl* **42**, 3825-3830.
Clements, J. E., Price, J. R., Neville, S. M. & Kepert, C. J. (2016). *Angew Chem Int Ed Engl* **55**, 15105-15109.

Collet, E., Boillot, M. L., Hebert, J., Moisan, N., Servol, M., Lorenc, M., Toupet, L., Buron-Le Cointe, M., Tissot, A. & Sainton, J. (2009). *Acta Crystallogr B* **65**, 474-480.
Collet, E., Buron-Le Cointe, M. & Cailleau, H. (2006). *Journal of the Physical Society of Japan* **75**, 011002.
Collet, E., Buron-Le Cointe, M., Lemée-Cailleau, M. H., Cailleau, H., Toupet, L., Meven, M., Mattauch, S., Heger, G. & Karl, N. (2001). *Physical Review B* **63**.
Collet, E., Lorenc, M., Cammarata, M., Guerin, L., Servol, M., Tissot, A., Boillot, M. L., Cailleau, H. & Buron-Le Cointe, M. (2012). *Chemistry-a European Journal* **18**, 2051-2055.
Collet, E., Moisan, N., Balde, C., Bertoni, R., Trzop, E., Laulhe, C., Lorenc, M., Servol, M., Cailleau, H., Tissot, A., Boillot, M. L., Graber, T., Henning, R., Coppens, P. & Buron-Le Cointe, M. (2012). *Physical Chemistry Chemical Physics* **14**, 6192-6199.
Collet, E., Watanabe, H., Brefuel, N., Palatinus, L., Roudaut, L., Toupet, L., Tanaka, K., Tuchagues, J. P., Fertey, P., Ravy, S., Toudic, B. & Cailleau, H. (2012). *Phys Rev Lett* **109**, 257206.
Coppens, P. (2015). *Struct Dyn* **2**, 020901.
Coppens, P., Benedict, J., Messerschmidt, M., Novozhilova, I., Graber, T., Chen, Y. S., Vorontsov, I., Scheins, S. & Zheng, S. L. (2010). *Acta Crystallographica Section A* **66**, 179-188.
Decurtins, S., Gutlich, P., Hasselbach, K. M., Hauser, A. & Spiering, H. (1985). *Inorganic Chemistry* **24**, 2174-2178.
Enachescu, C., Nishino, M., Miyashita, S., Boukheddaden, K., Varret, F. & Rikvold, P. A. (2015). *Physical Review B* **91**, 104102.
Fisher, M. E. & Selke, W. (1980). *Physical Review Letters* **44**, 1502-1505.
Fitzpatrick, A. J., Trzop, E., Muller-Bunz, H., Dirtu, M. M., Garcia, Y., Collet, E. & Morgan, G. G. (2015). *Chem Commun (Camb)* **51**, 17540-17543.
Goujon, A., Varret, F., Boukheddaden, K., Chong, C., Jeftić, J., Garcia, Y., Naik, A. D., Ameline, J. C. & Collet, E. (2008). *Inorganica Chimica Acta* **361**, 4055-4064.
Griffin, M., Shakespeare, S., Shepherd, H. J., Harding, C. J., Letard, J. F., Desplanches, C., Goeta, A. E., Howard, J. A. K., Powell, A. K., Mereacre, V., Garcia, Y., Naik, A. D., Muller-Bunz, H. & Morgan, G. G. (2011). *Angewandte Chemie-International Edition* **50**, 896-900.
Guerin, L., Hebert, J., Buron-Le Cointe, M., Adachi, S., Koshihara, S. Y., Cailleau, H. & Collet, E. (2010). *Phys Rev Lett* **105**, 246101.
Guionneau, P. (2014). *Dalton Transactions* **43**, 382-393.
Gutlich, P. & Hauser, A. (1990). *Coordination Chemistry Reviews* **97**, 1-22.
Halcrow, M. A. (2013). *Spin-crossover materials : properties and applications*. Wiley.
Harding, D. J., Phonsri, W., Harding, P., Murray, K. S., Moubaraki, B. & Jameson, G. N. L. (2015). *Dalton Transactions* **44**, 15079-15082.
Hauser, A. (1986). *Chemical Physics Letters* **124**, 543-548.
Huby, N., Guérin, L., Collet, E., Toupet, L., Ameline, J.-C., Cailleau, H., Roisnel, T., Tayagaki, T. & Tanaka, K. (2004). *Physical Review B* **69**.
Kim, C. D., Pillet, S., Wu, G., Fullagar, W. K. & Coppens, P. (2002). *Acta Crystallographica Section A* **58**, 5.
Koritsanszky, T. S. & Coppens, P. (2001). *Chemical Reviews* **101**, 1583-1628.
Kusz, J., Spiering, H. & Gutlich, P. (2001). *Journal of Applied Crystallography* **34**, 229-238.
Lemke, H. T., Kjær, K. S., Hartsock, R., Brandt van Driel, T., Chollet, M., Glownia, J. M., Song, S., Zhu, D., Pace, E., Matar, S. F., Nielsen, M. N., Benfatto, M., Gaffney, K. J., Collet, E. & Cammarata, M. (2017). *Nat. Commun.* **8**, 15342.
Leung, P. C. W., Emge, T. J., Beno, M. A., Wang, H. H., Williams, J. M., Petricek, V. & Coppens, P. (1985). *Journal of the American Chemical Society* **107**, 6184-6191.
Li, Z.-Y., Dai, J.-W., Shiota, Y., Yoshizawa, K., Kanegawa, S. & Sato, O. (2013). *Chemistry – A European Journal* **19**, 12948-12952.
Luan, J., Zhou, J., Liu, Z., Zhu, B., Wang, H., Bao, X., Liu, W., Tong, M.-L., Peng, G., Peng, H., Salmon, L. & Bousseksou, A. (2015). *Inorganic Chemistry* **54**, 5145-5147.
Marchivie, M., Guionneau, P., Howard, J. A. K., Chastanet, G., Letard, J. F., Goeta, A. E. & Chasseau, D. (2002). *Journal of the American Chemical Society* **124**, 194-195.
Marino, A., Buron-Le Cointe, M., Lorenc, M., Toupet, L., Henning, R., DiChiara, A. D., Moffat, K., Brefuel, N. & Collet, E. (2015). *Faraday Discuss* **177**, 363-379.
Money, V. A., Carbonera, C., Elhaïk, J., Halcrow, M. A., Howard, J. A. K. & Létard, J.-F. (2007). *Chemistry – A European Journal* **13**, 5503-5514.
Murnaghan, K. D., Carbonera, C., Toupet, L., Griffin, M., Dirtu, M. M., Desplanches, C., Garcia, Y., Collet, E., Letard, J. F. & Morgan, G. G. (2014). *Chemistry-a European Journal* **20**, 5613-5618.
Nicolazzi, W., Pillet, S. & Lecomte, C. (2008). *Physical Review B* **78**, 174401.
Ohwada, K., Fujii, Y., Takesue, N., Isobe, M., Ueda, Y., Nakao, H., Wakabayashi, Y., Murakami, Y., Ito, K., Amemiya, Y., Fujihisa, H., Aoki, K., Shobu, T., Noda, Y. & Ikeda, N. (2001). *Phys Rev Lett* **87**, 086402.
Ortega-Villar, N., Muñoz, C. M. & Real, A. J. (2016). *Magnetochemistry* **2**.
Paez-Espejo, M., Sy, M. & Boukheddaden, K. (2016). *J Am Chem Soc* **138**, 3202-3210.
Pillet, S., Bendeif, E.-E., Bonnet, S., Shepherd, H. J. & Guionneau, P. (2012). *Physical Review B* **86**, 064106
Pillet, S., Hubsch, J. & Lecomte, C. (2004). *The European Physical Journal B* **38**, 541-552.
Real, J. A., Gaspar, A. B. & Munoz, M. C. (2005). *Dalton Trans*, 2062-2079.
Reger, D. L., Little, C. A., Young, V. G. & Pink, M. (2001). *Inorganic Chemistry* **40**, 2870-2874.
Rigaku (2015). *CrysAlisPro 1.171.38.41 or 1.171.37.35h.*
Sato, T., Nishi, K., Iijima, S., Kojima, M. & Matsumoto, N. (2009). *Inorganic Chemistry* **48**, 7211-7229.
Shatruk, M., Phan, H., Chrisostomo, B. A. & Suleimenova, A. (2015). *Coordination Chemistry Reviews* **289–290**, 62-73.
Slimani, A., Boukheddaden, K. & Yamashita, K. (2015). *Physical Review B* **92**, 014111.
Spiering, H. & Willenbacher, N. (1989). *Journal of Physics: Condensed Matter* **1**, 10089.
Tissot, A., Bertoni, R., Collet, E., Toupet, L. & Boillot, M.-L. (2011). *Journal of Materials Chemistry* **21**, 18347.
Trzop, E., Buron-Le Cointe, M., Cailleau, H., Toupet, L., Molnar, G., Bousseksou, A., Gaspar, A. B., Real, J. A. & Collet, E. (2007). *Journal of Applied Crystallography* **40**, 158-164.
Trzop, E., Zhang, D., Pineiro-Lopez, L., Valverde-Munoz, F. J., Carmen Munoz, M., Palatinus, L., Guerin, L., Cailleau, H., Real, J. A. & Collet, E. (2016). *Angew Chem Int Ed Engl* **55**, 8675-8679.

Vieira, B. J. C., Coutinho, J. T., Santos, I. C., Pereira, L. C. J., Waerenborgh, J. C. & da Gama, V. (2013). *Inorganic Chemistry* **52**, 3845-3850.
Watanabe, H., Brefuel, N., Collet, E., Toupet, L., Tanaka, K. & Tuchagues, J. P. (2013). *Eur J Inorg Chem*, 710-715.
Watanabe, H., Tanaka, K., Bréfuel, N., Cailleau, H., Létard, J.-F., Ravy, S., Fertey, P., Nishino, M., Miyashita, S. & Collet, E. (2016). *Physical Review B* **93**.
Yamada, M., Hagiwara, H., Torigoe, H., Matsumoto, N., Kojima, M., Dahan, F., Tuchagues, J.-P., Re, N. & Iijima, S. (2006). *Chemistry – A European Journal* **12**, 4536-4549.
Zhang, D., Trzop, E., Valverde-Munoz, F. J., Piñeiro-López, L., Muñoz, M. C., Collet, E. & Real, J. A. (2017).
Zhang, D., Trzop, E., Valverde-Muñoz, F. J., Piñeiro-López, L., Muñoz, M. C., Collet, E. & Real, J. A. (2017). *Cryst Growth Des* **17**, 2736-2745.
Zhang, W. K., Alonso-Mori, R., Bergmann, U., Bressler, C., Chollet, M., Galler, A., Gawelda, W., Hadt, R. G., Hartsock, R. W., Kroll, T., Kjaer, K. S., Kubicek, K., Lemke, H. T., Liang, H. Y. W., Meyer, D. A., Nielsen, M. M., Purser, C., Robinson, J. S., Solomon, E. I., Sun, Z., Sokaras, D., van Driel, T. B., Vanko, G., Weng, T. C., Zhu, D. L. & Gaffney, K. J. (2014). *Nature* **509**, 345-348.